IEEE Robotics and Automation Letters (RA-L) paper, presented at ICRA 2024, Yokohama, Japan. Cite as RA-L paper.

Design and Optimization of an Origami-Inspired Foldable Pneumatic Actuator

Huaiyuan Chen, Yiyuan Ma, and Weidong Chen, *Member, IEEE*

***Abstract*—A novel origami-inspired foldable pneumatic actuator is proposed in this paper to satisfy the comprehensive requirements in wearable assistive application. The pneumatic actuator combines the origami structure of designed Quadrangular-Expand pattern and the foldable pneumatic bellow. Integrated origami structure regulates the motion of actuator with high contraction ratio and enables accurate modeling. The origami framework also improves the strength of bearing negative pressure, and thus can provide bidirectional actuation. The workflow including design, fabrication and mathematic modeling of the pneumatic actuator is presented in detail. Based on the actuator modeling, the multi-objective optimization for parameters using Genetic Algorithm is then conducted to obtain the trade-off design. The verifications for static characteristics of output torque, as well as the dynamic characteristics of power density, mechanical efficiency and frequency response, have been conducted. In summary, the proposed actuator is powerful and energy-efficient.**

***Index Terms*—Pneumatic actuator, origami-inspired, modeling, bidirectional actuation, parameter optimization.**

I. Introduction

PNEUMATIC actuators are attracting increasing interest for a number of promising properties [1]–[5]. The advantages of intrinsic compliance and high power-to-weight ratio bring pneumatic actuators closer to humans, such as the applications in wearable assistive devices. The main challenges of designing such actuators is satisfying comprehensive requirements of actuation mode, output force, actuation displacement, device size and actuation speed [6].

From perspective of pneumatic actuator structure design, the actuation mode should comply with the motion of human joints, i.e., rotation of flexion or extension. In such rotatory or bending pneumatic actuators, the origami-inspired actuators show advantages of regulated motion, customizable force capability and actuation linearity [7]–[14], compared with commonly-used McKibben-type actuators [15]–[18], fiber-reinforced actuators [19], [20] and bellow-type actuators [21]–[25]. Present origami-inspired actuators mainly utilize conventional origami patterns, such as Yoshimura pattern. Additive manufacturing has been applied for these actuators to improve the force capacity, compared with the paper-based actuators.

This work was supported by the National Key R&D Program of China under Grant 2020YFC2007500, and the Science and Technology Commission of Shanghai Municipality under Grant 20DZ2220400. (*Corresponding author: Weidong Chen*)

The authors are with School of Electronic Information and Electrical Engineering, the Department of Automation, Shanghai Jiao Tong university, and also with the Institute of Medical Robotics, Shanghai Jiao Tong university, Shanghai, China (e-mail: chynh123@sjtu.edu.cn, Ma-Yiyuan@sjtu.edu.cn, wdchen@sjtu.edu.cn)

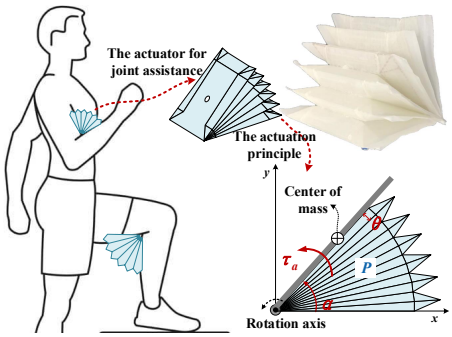

Fig. 1. Illustration of the actuator in wearable assistive applications.

However, the minimum wall thickness for additive manufacturing reduces the contraction/expansion ratio for origami-inspired actuator [11]. In addition, the single-chamber actuator structure will transfer to non-patterned structure at high air pressure, which would change the motion/force pattern [7]. Improvements from mentioned aspects will promote application of origami-inspired actuators to wearable assistive device.

The structure design realizes the main functions for design requirements. But to satisfy the comprehensive design requirements, further parameters determination should be conducted on the basis of structure design. Parameter optimization based on modeling is an effective method, compared with experimental parameters determination [26]. As for the rotatory origami-inspired actuators, the parameterized structure brings convenience to establish the mathematical model. The mathematical model can reflect a more direct relation between structure parameters and actuator characteristics in comparison with finite element method (FEM) [27]. In addition, mathematical modeling can make the parameter optimization more efficient. As for the application in wearable device, a more comprehensive optimization is necessary to achieve the trade-off for actuator size, output force, actuation displacement and actuation speed [28]. However, present researches mainly focus on the mechanical design and simple optimizations have been conducted for a few studies [9], [11], [29].

To sum up, this paper proposes a novel origami-inspired foldable pneumatic actuator for joint flexion/extension assistance in inner-side configuration, as is shown in Fig. 1. The actuator integrates the origami film from designed Quadrangular-Expand pattern with the bellow-type pneumatic actuator, which can achieve bidirectional actuation capacity, high contraction ratio and convenient modeling. The mathematical modeling based on the origami structure is derived for parameter optimization. And the multi-objective optimization

is conducted to satisfy the comprehensive design requirements in joint assistance. The contributions of this paper are:

1) The design of the actuator, especially the Quadrangular-Expand pattern, and layered fabrication are presented;

2) Parameters optimization using Genetic Algorithm (GA) is conducted on the basis of actuator mathematic modeling with the internal volume, output torque and pressure dynamics;

3) Experimental validation is conducted for actuator characterizations;

The rest of this paper is organized as follows: Section II presents the design and fabrication of proposed actuator. In Section III, the models of internal volume, output torque and actuator pressure dynamics are established. Section IV contains the effects of geometrical dimensions and parameters optimization using GA. Section V contains the evaluation of the static and dynamic characteristics for actuator. In Section VI and VII, discussions and conclusion are presented.

II. Design and Fabrication

The soft-rigid design for proposed pneumatic actuator is described firstly. The Quadrangular-Expand pattern for internal origami structure is then introduced to realize desired actuator deformation. Afterwards, the layered fabrication is presented.

A. Actuator Design

Structure design of the actuator should meet the ergonomics and provide appropriate assistive force to target joint. Our objective is to provide direct assistive torque for joint flexion/extension and therefore will lie at the inner-side of joint zone, as is illustrated in Fig. 1. This configuration avoids transformation of force type and provide a smooth distribution of contact pressure to minimize discomfort. To meet the mentioned aspects, the origami-inspired pneumatic actuator is designed from the bellow-type actuator with internally integrated rigid origami frame. Upon pressurization, the conventional bellow-type actuator generally presents fan-shape [21]. However, the soft foldable bellow-type actuator could only provide unidirectional actuation without bearing vacuum. In addition, it is difficult to establish the static and dynamic models of the pouches with unstructured shapes.

The key solution is to integrate a quadrangular frame into a single pouch of which the 2-dimensional (2D) quadrangular shape is illustrated in Fig. 2(a). When pressurized, the pressure on lateral two plates produces moments around the lowest hinge. The convex structure avoid a shift of configuration upon pressurization compared with the designs with concave structure [7], [10]. As for vacuum actuation, contraction will happen for the frame and reversed torque is generated.

Based on the 2D frame, the 3D quadrangular frame and the unfolded plane with crease line are shown in Fig. 2(b). Extra fold areas are compensated to make the prismatic frame align with peripheral lines of single pouch which are highlighted with light blue. For the compensated areas, the basic triangular sheets in designing origami pattern are utilized to determine the fold lines. The origami pattern is defined as Quadrangular-Expand pattern for the deformation mechanism is the quadrangular shape change, as is shown in Fig. 2(c).

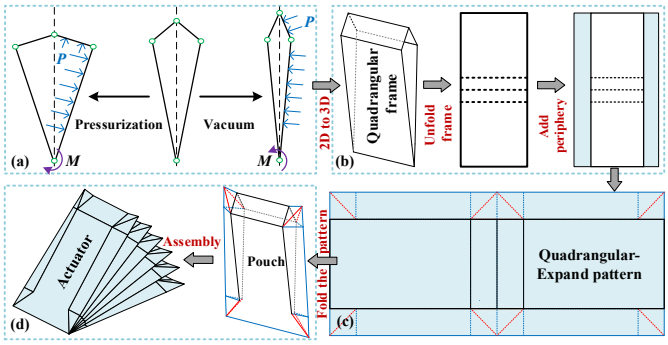

Fig. 2. Design of the actuator. (a) The 2D quadrangular frame for single pouch under pressurization/vacuum. (b) The 3D quadrangular frame from 2D frame. (c) Quadrangular-Expand pattern. (d) Single pouch and assembled actuator

The folded single pouch from Quadrangular-Expand pattern and the assembled actuator are finally obtained, shown in Fig. 2(d). The entire deformation process maintains structural shape. Therefore, parameterized description could be obtained.

B. Fabrication

With designed Quadrangular-Expand pattern, the actuator is constructed by integrating the frame into the soft bellow-type actuator. The ideal material for the frame should be thin, high-strength and can bear many times of folds. Therefore, the 0.3 mm polyvinyl chloride (PVC) film is selected. As for the external bellow, sealing fabric with high tensile strength is the applicable material and the thermoplastic polyurethanes (TPU) fabric is utilized. So the actuator mainly consists of two materials with low cost. The layered fabrication is then operated, as is shown in Fig. 3 and supplementary video.

STEP 1: The laser cutting is firstly used to construct the origami film. The cutting lines are constructed from three key parameters l_1, l_2, l_3. Dashed lines from pulse laser cutting for the creases reduce the bending stiffness and would induce the PVC film to fold in these lines. Upon a host of trials, the 20mm/s cutting speed, 14% of the rated power, 1.5mm pulse cutting interval and cutting length are selected (BF1390+, Kaitian). The prismatic area is cut out to reduce mechanical stresses from multiple folds intersection. And two holes are cut out to enable the air flow between adjacent chambers.

STEP 2: The double-side tape is used to adhere the processed PVC film into the 0.06mm TPU fabric with larger rectangular area. The TPU fabric contains two layers, i.e., the TPU layer and the high-strength Nylon layer. The TPU layer is set as inner side of air chamber which contacts PVC film.

STEP 3: The integrate sheet is folded in half to make TPU layer inward and the fabric along PVC periphery is heat-sealed to construct single chamber, as is illustrated in Fig. 3(c).

STEP 4: All the air chambers are connected by adhering highlighted areas in Fig. 3(d) with instant glue(5562, Youweite). It should be noted that the vents have to be aligned to guarantee fluent air flow. Two pneumatic connectors are installed in the lateral two holes to enable air flow and pressure measurement respectively.

IEEE Robotics and Automation Letters (RA-L) paper, presented at ICRA 2024, Yokohama, Japan. Cite as RA-L paper.

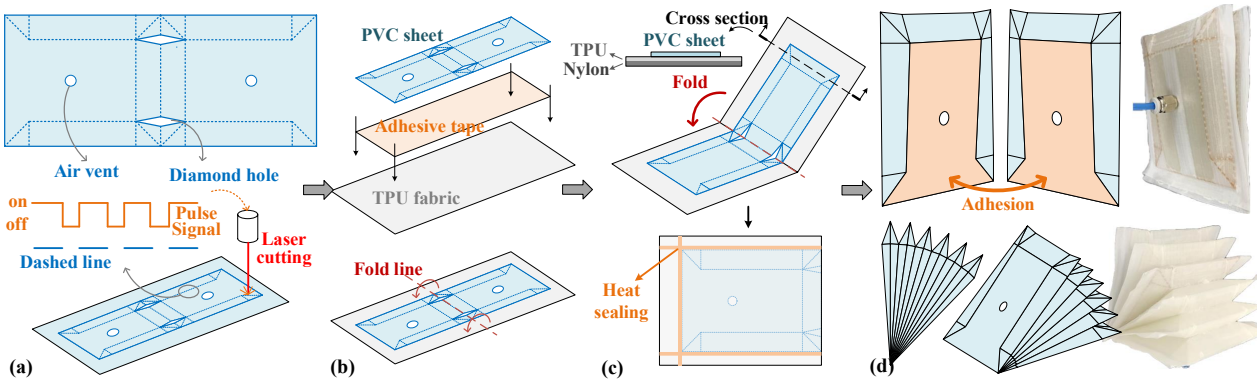

Fig. 3. Fabrication of the actuator. (a) Cut Quadrangular-Expand pattern for actuator framework out of PVC film. (b) Adhere the PVC film with origami pattern to the TPU fabric sheet with double-coating tape. (c) Heat-seal the folded composite sheet along the periphery. (d) Connect the chambers along highlighted adhesive areas with Nylon glue.

III. Modeling

The parameterization of origami structure enables mathematical modeling of proposed actuator. The internal volume model with respect to actuator parameters is firstly established. Afterwards, the pneumatic output torque is derived based on virtual work theory. And the pressure dynamics is analyzed on the basis of the internal volume model and torque model.

A. Internal Volume

For uniform deformation of the origami-inspired actuator, each fold could be seen as equivalent and one pouch is isolated to compute the volume. The single pouch is further decomposed into four parts for approximation, as is illustrated in Fig. 4(a). So, the volume v_0 can be computed as a sum of v_1, v_2, v_3 and v_4:

$$\begin{cases} v_1 = \frac{1}{2} l_1 l_2 \sin\theta \cdot (\sqrt{l_3^2 - l_1^2 \cdot \sin^2\theta} + l_1 \cos\theta) \\ v_2 = \frac{1}{3} l_1 l_3 \sin\theta \cdot \sqrt{l_3^2 - l_1^2 \cdot \sin^2\theta} \\ v_3 = \frac{1}{3} l_1 \sin\theta (l_3^2 - l_1^2 \cdot \sin^2\theta) \\ v_4 = \frac{1}{6} l_1^2 \sin\theta \cos\theta (l_3 + 2\sqrt{l_3^2 - l_1^2 \cdot \sin^2\theta}) \end{cases} \tag{1}$$

$$v_0 = 2 \cdot (v_1 + v_2 + v_3 + v_4) \tag{2}$$

where θ is defined as the actuation angle of one pouch. The simplification with $\sin\theta \approx \theta$ and $\cos\theta \approx 1$ is conducted when θ is relatively small. Larger θ would affects the approximation accuracy, thus the analysis would be mainly discussed within $20°$ for better performance prediction. Then the volume model can be simplified for later calculation:

$$v_0 = f(l_1, l_2, l_3) \cdot \theta + g(\theta, l_1, l_2, l_3) \tag{3}$$

$$\begin{cases} f(l_1, l_2, l_3) = l_1^2 l_2 + \frac{2}{3} l_1 l_3^2 + \frac{1}{3} l_1^2 l_3 \\ g(\theta, l_1, l_2, l_3) = (l_1 l_2 + \frac{2}{3} l_1 l_3 + \frac{2}{3} l_1^2) \cdot \theta \\ \qquad \cdot \sqrt{l_3^2 - l_1^2 \theta^2} - \frac{2}{3} l_1^3 \theta^3 \end{cases} \tag{4}$$

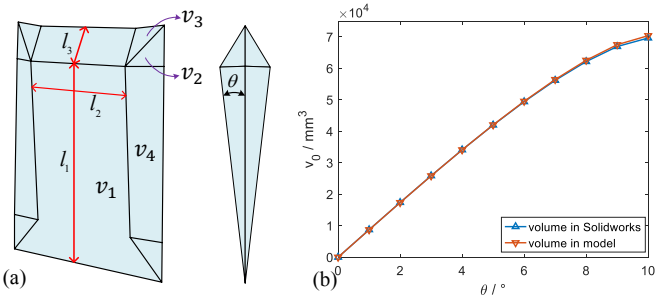

Fig. 4. (a) Parameterization of the origami-inspired actuator and volume V divided with v_1, v_2, v_3 and v_4. (b) The volume of pneumatic actuator based on simplified volume model and ground-truth in Solidworks.

where f constitutes the linear term of v_0 with respect to θ, g is the nonlinear term. To evaluate the accuracy of simplified volume model, the volume in Solidworks (Dassault Systems) is utilized as ground truth for comparison. The pouch volumes from two approaches are shown in Fig. 4(b). The result shows high consistency between simplified model and ground truth. A linear relation between volume and θ can be observed within specific range. This linear relation is the contribution of $f(l_1, l_2, l_3)$ in Eq. (3). For the actuator with n pouches, the actuator angle is $\alpha = 2n\theta$ and overall volume is described as:

$$V = n \cdot v_0 \tag{5}$$

The pouch number will be set according to the demand angle range to provide actuation redundancy. Based on volume model, the simplified process benefits the derivation of torque.

B. Output Torque

To analyze the characteristics of designed pneumatic actuator, the static torque function of geometrical parameters and driving pressure is established. The virtual work theory is utilized to derive the torque function. In the equilibrium state, the virtual angle change and virtual volume change of the actuator are assumed to be $\delta\alpha$ and δV. The virtual work equation [21] is derived as:

$$\delta W_e + \delta W + \delta W_0 = 0 \tag{6}$$

with

$$\begin{cases} \delta W_e = -\tau_e \cdot \delta\alpha \\ \delta W = P \cdot \delta V - k\alpha \cdot \delta\alpha \\ \delta W_0 = -P_0 \cdot \delta V \end{cases} \tag{7}$$

where W_e, W and W_0 are the virtual work generated by the external torque, the actuator including internal absolute pressure P and stiffness force, and the atmosphere pressure P_0, respectively. k is the actuator stiffness. By substituting Eq. (6) and Eq. (7), the expression for generated output torque by actuator τ_a is obtained as follows:

$$\tau_a = \tau_e = (P - P_0) \cdot \frac{\delta V}{\delta\alpha} - k\alpha = p \cdot \frac{\delta V}{\delta\alpha} - k\alpha \tag{8}$$

where p is the gauge pressure. With the transformation $\delta V = (dV(\alpha)/d\alpha) \cdot \delta\alpha$, $\alpha = n \cdot (2\theta)$ and $V(\alpha) = n \cdot v_0$, the torque τ from pneumatic pressure is obtained:

$$\tau = p \cdot \frac{\delta V}{\delta\alpha} = p \cdot \frac{dV(\alpha)}{d\alpha} = p \cdot \frac{dv_0}{2d\theta} = p \cdot (\frac{f}{2} + \frac{dg}{2d\theta}) \tag{9}$$

According to the internal volume model in Eq. (2), the static output torque from pressure can be further described as:

$$\begin{aligned} \tau =& p \cdot [(\frac{1}{2}l_1 l_2 + \frac{1}{3}l_1 l_3 + \frac{1}{3}l_1^2)(\sqrt{l_3^2 - l_1^2\theta^2} + \frac{l_1^2\theta^2}{\sqrt{l_3^2 - l_1^2\theta^2}}) \\ &+ \frac{1}{2}l_1^2 l_2 + \frac{1}{3}l_1 l_3^2 + \frac{1}{6}l_1^2 l_3 - l_1^3\theta^2] \end{aligned} \tag{10}$$

From the equation, the desired output torque under specific geometry can be obtained by adjusting the internal pressure. A desired profile for $\tau - p - \theta$ or $\tau - p - \alpha$ curves can be obtained by designing the geometrical parameter in advance.

C. Pressure Dynamics

According to the output torque $\tau = p \cdot dV/d\alpha$, the required torque can be obtained through pressure regulating. As for the entire pneumatic system, the pressure is regulated through air flow. Therefore, the pressure dynamics for the actuator can be described as [30]:

$$\dot{P} = (\gamma RT\dot{m} - \gamma P\dot{V})/V \tag{11}$$

where $\dot{m}$ is the air mass flow, R is the universal gas constant, T represents the gas temperature, V is the volume, γ is the ratio of specific heats. As for the air mass flow, it's a function of air supply and valve features, and can be modeled based on the related parameters as follows [30]:

$$\dot{m}(P_u, P_d) = A \cdot \dot{m}_0(P_u, P_d) \tag{12}$$

$$\dot{m}_0(p_u, p_d) = \begin{cases} \sqrt{\frac{\gamma}{RT}\left(\frac{2}{\gamma+1}\right)^{\left(\frac{\gamma+1}{\gamma-1}\right)}} C_f P_u \quad , & \text{if} \quad \frac{P_d}{P_u} \le C_r \\ \sqrt{\frac{2\gamma}{RT(\gamma-1)}} \sqrt{1 - \left(\frac{P_d}{P_u}\right)^{\left(\frac{\gamma-1}{\gamma}\right)}} \left(\frac{P_d}{P_u}\right)^{\left(\frac{1}{\gamma}\right)} C_f P_u, & \text{other} \end{cases} \tag{13}$$

where $\dot{m}_0$ represents the maximum mass flow for given pressures with a fully opened valve. P_u and P_d denote the upstream and downstream pressure of actuator. C_f is the discharge coefficient of valve and C_r is the pressure ratio determining the flow state. A is the proportional valve command to control real air flow and $A = 1$ means valve fully open.

For the joint driven by single pneumatic actuator, the dynamic behaviour is described as:

$$J\ddot{\alpha} + b\dot{\alpha} + (k + k_j)\alpha = p\frac{dV_\alpha}{d\alpha} + \tau_e \tag{14}$$

where J is the moment of inertia calculated from mass distribution, k is the actuator stiffness, k_j is the joint stiffness, b is the joint damping and τ_e is the torque from external force.

For given actuation conditions, the dynamic response can be obtained through Eq. (11)-(14). The dynamic process mainly depends on the input air flow and actuator configuration. For constant air flow, the dynamic response is determined by the actuator shape. Reduced actuator size could give rise to higher response for given load based on comparative analysis [30].

IV. Parameters Optimization

On the basis of mathematical modeling, the parameters optimization is conducted. The effects of geometrical dimensions are firstly analyzed to provide prior information for optimization. The multi-objective optimization using GA is then constructed to obtain the trade-off between output torque and dynamic response.

A. Effects of Geometrical Dimensions

l_1, l_2, l_3 are three key parameters for the actuator. l_2 mainly reflects the width of actuator and can be treated as a linear coefficient. While for l_1 and l_3, mutual effects can be found from volume and torque model. To have a comprehensive understanding of the actuator characteristics, 5 sets of l_1 and l_3 with constant l_2=70mm are selected for analysis on reference of [21]: Set1, l_1=100mm and l_3=20mm; Set2, l_1=100mm and l_3=30mm; Set3, l_1=100mm and l_3=40mm; Set4, l_1=90mm and l_3=20mm; Set5, l_1=80mm and l_3=20mm. With fixed number of segments 6, the internal volume in range of motion (ROM) and torque coefficient are depicted in Fig. 5.

As is shown in Fig. 5(a), the ROM is mainly determined by the ratio r=l_3/l_1. Larger r will generate larger ROM. The largest ROM of around $250°$ is obtained for Set3. Within respective ROM, the volumes show similar characteristics that linear feature with α plays a main role within specific range and then the increases gradually ease up. Larger volume is found with larger l_1 and l_3. And l_3 make more contributions to volume change. The torque coefficients are described in Fig. 5(b). It's obvious that larger l_1 or l_3 will generate larger torque for given pressure. This relation corresponds to the volume characteristics. But larger l_1 or l_3 would enlarge the actuator size and the trade-off has to be made.

IEEE Robotics and Automation Letters (RA-L) paper, presented at ICRA 2024, Yokohama, Japan. Cite as RA-L paper.

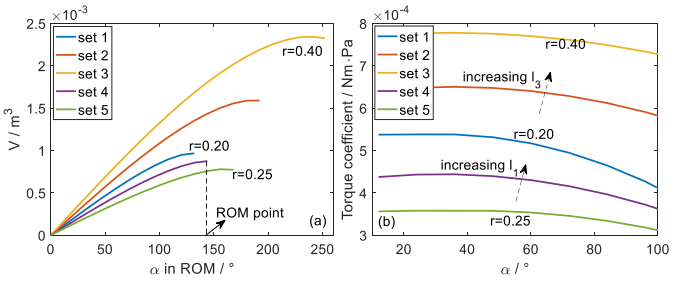

Fig. 5. Parameter effects. (a) The volume with different sets of parameters. (b) The torque coefficient with different sets of parameters.

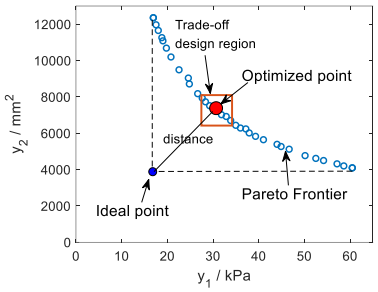

Fig. 6. Pareto front of the multi-objective optimization.

B. Optimization based on Genetic Algorithm

Design requirements for different applications can be satisfied through adjustment of the parameters. The application in elbow assistance is taken as a case study, of which the movement corresponds to the actuation. The design requirements are set with 100° for ROM and 7Nm for torque [31], [32].

According to internal volume model and torque model, the core linear relation between volume and angle can be found within specific range. Therefore, the main linear term f is analyzed for parameter optimization. According to the effects of geometrical dimensions, l_1 and l_3 are selected as the optimization variables. And l_2 is set as 50mm empirically. For l_1 and l_3, larger size will produce higher torque at specific actuating pressure, or lower actuating pressure at specific torque. But for given load condition, larger size would slow the dynamic response for larger air flow consume. Therefore, to achieve trade-off design between the actuating pressure and actuator size, i.e., output torque and dynamic response, the multi-objective optimization is constructed as:

$$\begin{aligned} \min \quad & y_1 = \frac{M}{\frac{1}{2}l_1^2 l_2 + \frac{1}{3}l_1 l_3^2 + \frac{1}{6}l_1^2 l_3} \\ & y_2 = (l_2 + 2l_3) \cdot l_1 \\ s.t. \quad & 5mm \le l_3 < l_1 \\ & 10mm < l_1 \\ & p = y_1 < 2bar \\ & l_2 = 50mm \\ & \alpha = 2n\theta \ge 100^\circ \end{aligned} \tag{15}$$

where y_1 represents the pressure for requiring torque M=7Nm, y_2 is the sectional area of actuator. Smaller y_1 means lower actuating pressure, which can benefit the miniaturization of air source. The pouch number n is selected as 6 empirically.

The multi-objective optimization can be solved by finding the Pareto front which consists of all acceptable optimal sets [33]. Genetic Algorithm (GA) is well suited to find Pareto optimal sets, as a population-based method [34]. Simultaneously searching different regions of a solution space enables GA to find a diverse set of solutions. In addition, GA for multi-objective optimization do not require the user to prioritize or weigh objectives. Therefore, this multi-objective optimization was completed with GA [35]. The constructed optimization was conducted in Matlab 2016. The population size was set with 50 and function tolerance was selected as 0.001.

TABLE I
THE OPTIMIZED PARAMETERS AND DESIGN OBJECTIVES

Index	l_1	l_2	l_3	ROM	P
Value	80mm	50mm	15mm	129°	30kPa

Several trials have been conducted and only small deviations of the results were found which showed that the optimization was reliable and repeatable. The computing time was allocated from 5-10min and the stop iterations for convergence was from 100-150. One general Pareto front of the optimization was obtained in Fig. 6. The front shows that the lower values of y_2 could be achieved for larger y_1. The actuator can meet different tasks by choosing from maximal size design scheme to maximal pressure design scheme according to the relative importance. Here, a balanced design between y_1 and y_2 would be selected based on the ideal point which is often defined as the reference point [36]:

$$\boldsymbol{x}_{\text{ideal}} = [\ \min(y_1) \quad \min(y_2)\ ] \tag{16}$$

This ideal point can not be reached in a multi-objective optimization problem because these objectives cannot be minimized simultaneously. The final balanced solution was defined as the point in Pareto with the shortest distance to the ideal point [37], which is depicted with red point. For the point, l_1 ≈80mm and l_3 ≈15mm. In addition, for the solution sets highlighted in rectangular box around the obtained point, the ranges are obtained with 75mm< l_1 <80mm and 10mm< l_3 <15mm. Therefore, the final parameters with l_1=80mm and l_3=15mm were determined. The parameters are shown in Table I. With the optimized parameters, the ROM is up to 129° and the actuating pressure for 7Nm is 30kPa. The performance satisfies the design requirements.

V. VERIFICATION

The actuator with optimized parameters is fabricated for verification. The static torque with respect to pressure and actuator configuration are verified. In addition, the dynamic characteristics including power density, mechanical efficiency and frequency response are analyzed.

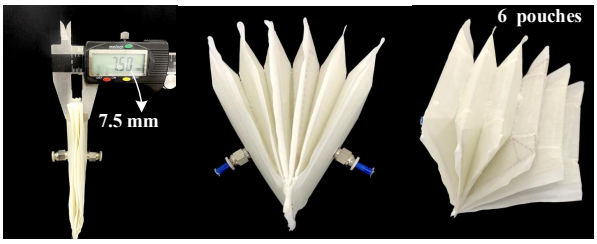

Fig. 7. The fabricated pneumatic actuator with optimized parameters

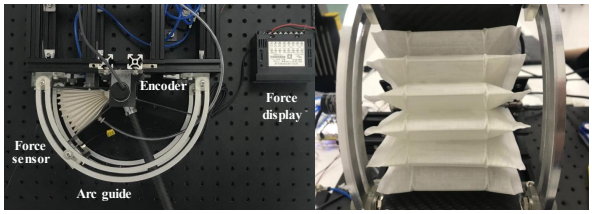

Fig. 8. Experimental setup for testing output torque.

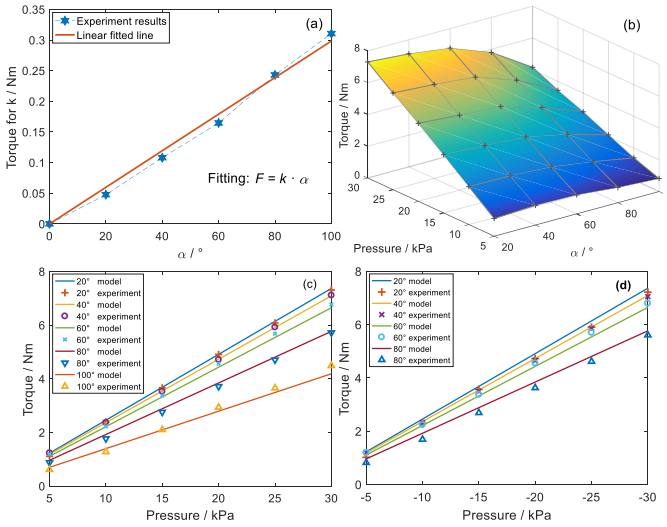

Fig. 9. Static torque tests. (a) The torque for actuator stiffness and the linear fitting with angle α. (b) The static torque at different actuator angle α and internal pressure. (c) The torque at specific angle with different positive pressure. (d) The torque at specific angle with different negative pressure.

A. Actuator for Experiments

The pneumatic actuator with optimized parameters is shown in Fig. 7. Upon pressurization, the actuator expands with fan-shape. With composed six pouches, the thickness of pneumatic actuator is 7.5mm and the initial angle α is around $10°$. In consideration of the maximum angle $129°$, the actuator has a contraction ratio of 92.3%. In addition, the mass of actuator is only 60g, which can benefit high power-to-weight ratio.

B. Static Characteristics

The platform for testing static torque consists of a hinge, semicircle guide, encoder and force sensor, as is illustrated in Fig. 8. The pressure controller (VP50 plus, Elveflow) was utilized to provide positive and negative pressure for pneumatic actuator. The angle α was measured by an encoder (Omron, EA62). A semicircle guide was utilized to fix the force sensor (SBT650, SIMBATOUCH) at different angles. The output torque was calculated from force multiplied by moment arm. The static torque for actuator was measured for variable internal gauge pressure p at different fixed angle α. Initial angle of the actuator is around $10°$ for thickness.

The torque for actuator stiffness was obtained when p=0kPa, as is shown in Fig. 9(a). A nearly linear relation with k=0.17Nm/rad could be observed. The stiffness mainly came from fold line of PVC origami film. The relation for $\tau - p - \alpha$ under positive pressure is depicted in Fig. 9(b). The torque increased with internal pressure, but reduced with the actuator angle α. The torque extracting stiffness at constant angle with different positive pressures is described in Fig. 9(c). The torque was up to 7.3Nm at 30 kPa/20°. For fixed angle, the torque showed a linear relation with the pressure. However, the torque reduced for increasing actuator angle at constant pressure, which can be explained by the nonlinear term g in Eq. (4). Slight deviations were observed between the experimental and model results, possibly caused by the fabrication process. It should be noted that higher torque can be obtained with higher pressures and the maximum pressure was obtained around 140kPa. The major concern is actuation capacity in same situations, not extreme actuation capacity.

The torque at negative pressure is shown in Fig. 9(d). A similar result to that in positive pressure was found. The torque was up to 7.0Nm at -30kPa/20°. But complete data were not captured for the tests at 100°/-30kPa. For the deformation of configuration under this situation influenced the desired torque pattern. Increment of pouch numbers can be a solution to improve the performance under negative pressure. In consideration of maximum pressure, the actuator satisfies the demand of case study for elbow assistance. And the actuating pressure at 7Nm matches the optimization result.

C. Dynamic Characteristics

The response tests for dynamic characteristics are conducted on the rotational joint, as is shown in Fig. 10(a). The damping and stiffness of this joint is neglected. The load-lifting task was completed through pulley mechanisms for transferring tension force to torque. Different loads with 1kg, 2kg and 5kg were used. A pressure sensor (XGZ, CFSensor) was utilized to measure the pressure. The tests were conducted under 300kPa and -80kPa with valve (VQ100, SMC) fully-open, respectively. In consideration of the initial state and safe motion range, the angle range was $10°$-$100°$ for positive pressure, and $80°$-$10°$ for negative pressure. The pneumatic system is shown in Fig. 10(b). Valve 1 was responsible for inflation, while valve 2 for deflation. In addition, the simulations of pressure dynamics (Eq. (12)-(14)) were conducted to compare with experiments. The parameters in modeling are shown in Table. II. Apart from load-lifting task, the frequency response was also tested by controlling the valves with square waves [38] ranging from 0.2 to 6Hz and the angle range were measured.

The angle α response for different load-lifting tests and the simulation result are shown in Fig. 11(a). Heavier loads from 1kg to 5kg gave rise to longer response time, from

IEEE Robotics and Automation Letters (RA-L) paper, presented at ICRA 2024, Yokohama, Japan. Cite as RA-L paper.

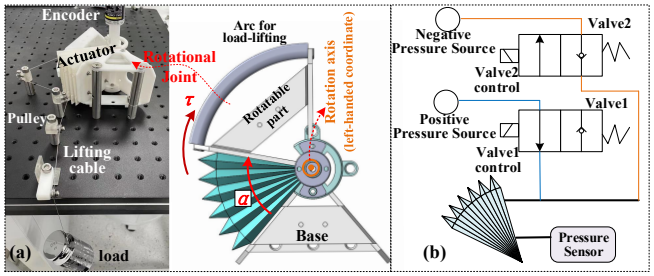

Fig. 10. Experimental setup for dynamic characteristics. (a) The load-lifting test in the joint. (b) The pneumatic system to drive the actuator.

TABLE II
PARAMETERS USED IN MODEL

Parameter	Value	Unit	Parameter	Value	Unit
γ	1.4		C_r	0.22	
R	0.287	kJ/(kgK)	C_f	0.15	
T	293	K			

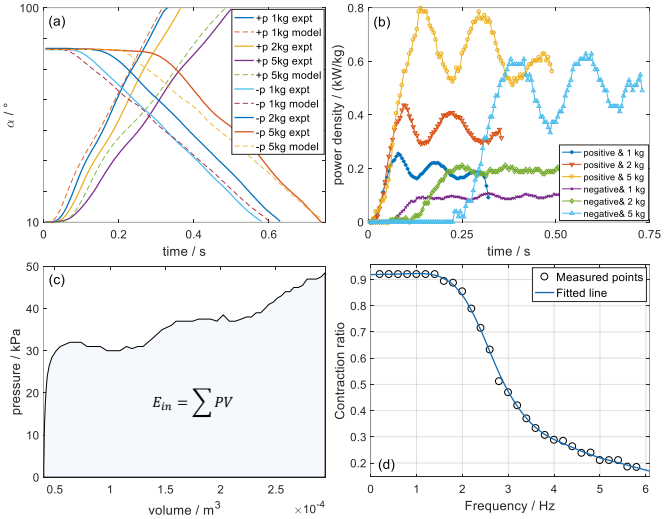

Fig. 11. Dynamic characteristics. (a) The angle response at load-lifting tests for experiment and simulation. (b) The power density for the actuator. (c) The pressure-volume relation for input energy of actuator at 5kg-lifting test. (d) The frequency response.

0.3s to 0.5s for pressurization and from 0.6s to 0.8s for vacuum to reach settle state. More time was also needed to overcome heavier load for onset of movement, such as 0.3s for lifting 5kg under vacuum. In addition, faster response could be found under positive pressurization compared with negative pressure for larger air flow. The simulations showed almost same characteristics with experiments, such as the fluctuations.

The corresponding power density ρ [39] is calculated with:

$$\rho = \frac{W_a}{m_a} = \frac{m_{load} \cdot g \cdot v_{load}}{m_a} \tag{17}$$

where W_a is mechanical power for lifting loads, m_a is the actuator mass, m_{load} is the load mass, g is the gravitational acceleration and v_{load} is the velocity of load which is calculated from angle response. The power density is shown in Fig. 11(b). Faster response for positive pressurization gave rise to higher power density at the same load. The peak power density of 0.8 kW/kg was obtained for positive pressure and 5kg-load.

The mechanical efficiency η [39] is calculated with:

$$\eta = \frac{E_{out}}{E_{in}} = \frac{m_{load} \cdot g \cdot h_{load}}{\Sigma PV} \tag{18}$$

where E_{in} is the input energy (the shaded area in Fig. 11(c)), E_{out} is the output energy, P is the internal pressure of actuator and V is the volume. The volume was obtained from volume-angle model (2). The peak mechanical efficiency was 41.9% which is relatively high in pneumatic systems [40].

The motion range in form of contraction ratio is described in Fig. 11(d). The motion range reduced at high frequencies and the cut-off frequency was 2-3 Hz, which is consistent with actual muscle [38]. And the actuator was capable of fully inflating, but incapable of fully deflating, which was restricted by the mass flow of negative pressure and small valve orifice.

According to the dynamic results, the proposed actuator is powerful and energy efficient. The optimized parameters reduces the size of actuator, but increases the driving capacity at specific pressure. Therefore, the actuator could have faster response, i.e., higher power density. In summary, the actuator with optimized parameters matches the demand of case study for elbow assistance.

VI. Discussions

To satisfy comprehensive requirements in wearable assistive application, the structure design and parameter optimization have been sequentially conducted for proposed actuator.

The internal origami frame from Quadrangular-Expand pattern improves the actuator on bidirectional actuation for joint flexion and extension assistance, compared with the soft bellow-type actuators without capacity of bearing vacuum [21], [24]. The origami structure also enables more direct and convenient modeling than soft bellows, which will benefit parameter determination and control analysis. And the layered fabrication can provide the actuator with larger contraction ratio and lighter mass, compared with those foldable origami-inspired actuators using additive manufacture [10], [11]. Larger contraction ratio will benefit the joint assistance range, such as 0.92 with 10°-129° for proposed actuator versus 0.5 with 60°-120° for actuator in [10]. The advantages of proposed actuator are reflected from a comprehensive perspective, not in specific index for which different designs have specific objectives and structure parameters.

The Pareto front for the multi-objective optimization is obtained using GA to provide acceptable optimal sets. The final balanced solution between output torque and dynamic response is selected in Pareto front. Above the Pareto front, the feasible points, but not optimal, can be found, such as the set with l_1=60mm and l_3=30mm. This feasible set can achieve 5.4Nm torque at 20°/30kPa and 0.5s response time under 1kg load through modeling, which shows that the optimized actuator can have better performance. It's worth noting that the actuator can meet different tasks by choosing from maximal size design to maximal pressure design scheme according to relative importance. Other tasks may be studied in the future.

VII. Conclusion

A novel origami-inspired foldable pneumatic actuator is proposed in this paper for wearable assistive application. The design, fabrication and mathematic modeling of the pneumatic actuator is presented. The parameters optimization is conducted based on the modeling to achieve trade-off between output torque and dynamic response using GA. The experimental results show that the designed origami-inspired actuator with optimized parameters can satisfy the comprehensive requirements in elbow assistive device.

Future work is designing the wearable exoskeleton based on proposed actuator. The high power-to-weight ratio, power density and mechanical efficiency benefits the lightweight and wearable designs. The bidirectional drive capacity could provide both flexion and extension for human joints.

References

[1] B. Gorissen, D. Reynaerts, S. Konishi, K. Yoshida, J.-W. Kim, and M. De Volder, "Elastic inflatable actuators for soft robotic applications," *Adv. Mater.*, vol. 29, no. 43, p. 1604977, 2017.

[2] P. Polygerinos, N. Correll, S. A. Morin, B. Mosadegh, C. D. Onal, K. Petersen, M. Cianchetti, M. T. Tolley, and R. F. Shepherd, "Soft robotics: Review of fluid-driven intrinsically soft devices; manufacturing, sensing, control, and applications in human-robot interaction," *Adv. Eng. Mater.*, vol. 19, no. 12, p. 1700016, 2017.

[3] G. M. Whitesides, "Soft robotics," *Angew. Chemie. Int. Edit.*, vol. 57, no. 16, pp. 4258–4273, 2018.

[4] D. Rus and M. Tolley, "Design, fabrication and control of soft robots," *Nature*, vol. 521, pp. 467–75, 05 2015.

[5] F. Xu and H. Wang, "Soft robotics: Morphology and morphology-inspired motion strategy," *IEEE/CAA J. Automatica. Sinica*, vol. 8, no. 9, pp. 1500–1522, 2021.

[6] T. Jin, L. Li, T. Wang, G. Wang, J. Cai, Y. Tian, and Q. Zhang, "Origami-inspired soft actuators for stimulus perception and crawling robot applications," *IEEE Trans. Robot.*, vol. 38, no. 2, pp. 748–764, 2022.

[7] X. Zou, T. Liang, M. Yang, C. LoPresti, S. Shukla, M. Akin, B. T. Weil, S. Hoque, E. Gruber, and A. D. Mazzeo, "Paper-based robotics with stackable pneumatic actuators," *Soft Robot.*, vol. 9, no. 3, pp. 542–551, 2022.

[8] S. Liu, H. Wu, Y. Yang, and M. Y. Wang, "Parallel-motion thick origami structure for robotic design," in *Proc. IEEE Int. Conf. Robot. Autom.*, 2020, pp. 934–939.

[9] L. Paez, G. Agarwal, and J. Paik, "Design and analysis of a soft pneumatic actuator with origami shell reinforcement," *Soft Robot.*, vol. 3, no. 3, pp. 109–119, 2016.

[10] J. Yi, X. Chen, C. Song, J. Zhou, Y. Liu, S. Liu, and Z. Wang, "Customizable three-dimensional-printed origami soft robotic joint with effective behavior shaping for safe interactions," *IEEE Trans. Robot.*, vol. 35, no. 1, pp. 114–123, 2019.

[11] S. Seo, W. Park, D. Lee, and J. Bae, "Origami-structured actuating modules for upper limb support," *IEEE Robot. Automat. Lett.*, vol. 6, no. 3, pp. 5239–5246, 2021.

[12] D. Kim, "Design and analysis of an origami-structured actuator for back-driveability and power amplification," *IEEE/ASME Trans. Mechatronics*, vol. 24, no. 3, pp. 1002–1010, 2019.

[13] A. Zaghloul and G. M. Bone, "Origami-inspired soft pneumatic actuators: Generalization and design optimization," *Actuators*, vol. 12, no. 2, 2023.

[14] W. Yue, J. Qi, X. Song, S. Fan, G. Fortino, C.-H. Chen, C. Xu, and H. Ren, "Origami-inspired structure with pneumatic-induced variable stiffness for multi-dof force-sensing," *Sensors*, vol. 22, no. 14, 2022.

[15] B. Tondu, "Modelling of the mckibben artificial muscle: A review," *J. Intel. Mat. Syst. Str*, vol. 23, no. 3, pp. 225–253, 2012.

[16] M. Zhang, J. Huang, Y. Cao, C.-H. Xiong, and S. Mohammed, "Echo state network-enhanced super-twisting control of passive gait training exoskeleton driven by pneumatic muscles," *IEEE/ASME Trans. Mechatronics*, pp. 1–12, 2022.

[17] A.-F. Hassanin, D. Steve, and N.-M. Samia, "A novel, soft, bending actuator for use in power assist and rehabilitation exoskeletons," in *Proc. IEEE/RSJ Int. Conf. Intell. Robots Syst.*, 2017, pp. 533–538.

[18] J. Wang, Y. Fei, and W. Chen, "Integration, sensing, and control of a modular soft-rigid pneumatic lower limb exoskeleton," *Soft Robot.*, vol. 7, no. 2, pp. 140–154, 2020.

[19] F. Connolly, C. J. Walsh, and K. Bertoldi, "Automatic design of fiber-reinforced soft actuators for trajectory matching," *Proc. Natl. Acad. Sci. USA*, vol. 114, no. 1, pp. 51–56, 2017.

[20] K. Ma, Z. Jiang, S. Gao, X. Cao, and F. Xu, "Design and analysis of fiber-reinforced soft actuators for wearable hand rehabilitation device," *IEEE Robot. Automat. Lett.*, vol. 7, no. 3, pp. 6115–6122, 2022.

[21] J. Fang, J. Yuan, M. Wang, L. Xiao, J. Yang, Z. Lin, P. Xu, and L. Hou, "Novel accordion-inspired foldable pneumatic actuators for knee assistive devices," *Soft Robot.*, vol. 7, no. 1, pp. 95–108, 2020.

[22] R. Natividad, M. Del Rosario, P. C. Chen, and C.-H. Yeow, "A reconfigurable pneumatic bending actuator with replaceable inflation modules," *Soft Robot.*, vol. 5, no. 3, pp. 304–317, 2018.

[23] T. M. Miller-Jackson, R. F. Natividad, D. Y. L. Lim, L. Hernandez-Barraza, J. W. Ambrose, and R. C. H. Yeow, "A wearable soft robotic exoskeleton for hip flexion rehabilitation," *Frontiers. Robot. AI*, vol. 9, 2022.

[24] C. M. Thalman, Q. P. Lam, P. H. Nguyen, S. Sridar, and P. Polygerinos, "A novel soft elbow exosuit to supplement bicep lifting capacity," in *Proc. IEEE/RSJ Int. Conf. Intell. Robots Syst.*, 2018, pp. 6965–6971.

[25] Y. Wang, S. Kokubu, Z. Zhou, X. Guo, Y.-H. Hsueh, and W. Yu, "Designing soft pneumatic actuators for thumb movements," *IEEE Robot. Autom. Lett.*, vol. 6, no. 4, pp. 8450–8457, 2021.

[26] F. Chen and M. Y. Wang, "Design optimization of soft robots: A review of the state of the art," *IEEE Robot. Autom. Mag*, vol. 27, no. 4, pp. 27–43, 2020.

[27] P. Huy Nguyen and W. Zhang, "Design and computational modeling of fabric soft pneumatic actuators for wearable assistive devices," *Sci. Rep.*, vol. 10, 06 2020.

[28] S. Joshi and J. Paik, "Multi-dof force characterization of soft actuators," *IEEE Robot. Automat. Lett.*, vol. 4, no. 4, pp. 3679–3686, 2019.

[29] Z. Zhang, G. Chen, H. Wu, L. Kong, and H. Wang, "A pneumatic/cable-driven hybrid linear actuator with combined structure of origami chambers and deployable mechanism," *IEEE Robot. Automat. Lett.*, vol. 5, no. 2, pp. 3564–3571, 2020.

[30] S. Joshi, H. Sonar, and J. Paik, "Flow path optimization for soft pneumatic actuators: Towards optimal performance and portability," *IEEE Robot. Automat. Lett.*, vol. 6, no. 4, pp. 7949–7956, 2021.

[31] J. A. French, C. G. Rose, and M. K. O'Malley, "System characterization of mahi exo-ii: A robotic exoskeleton for upper extremity rehabilitation," in *ASME Dyn. Syst. Contr. Conf.*, vol. 3, 10 2014.

[32] J. P. Haverstock, G. J. King, G. S. Athwal, J. A. Johnson, and G. D. G. Langohr, "Elbow motion patterns during daily activity," *J. Shoulder. Elb. Surg*, vol. 29, no. 10, pp. 2007–2014, 2020.

[33] P. Ngatchou, A. Zarei, and A. El-Sharkawi, "Pareto multi objective optimization," in *Proc. Int. Conf. Intel. Syst. Appl. Power Syst.*, pp. 84–91, 2005.

[34] A. Konak, D. W. Coit, and A. E. Smith, "Multi-objective optimization using genetic algorithms: A tutorial," *Reliab. Eng. Syst. Safe*, vol. 91, no. 9, pp. 992–1007, 2006.

[35] K. Deb, *Multiobjective Optimization Using Evolutionary Algorithms. Wiley, New York*, pp. 3–34. 01 2001.

[36] M. Ehrgott and D. Tenfelde-Podehl, "Computation of ideal and nadir values and implications for their use in mcdm methods," *Eur J. Oper. Res*, vol. 151, no. 1, pp. 119–139, 2003.

[37] F. Bre and V. D. Fachinotti, "A computational multi-objective optimization method to improve energy efficiency and thermal comfort in dwellings," *Energ. Buildings*, vol. 154, pp. 283–294, 2017.

[38] D. Kingsley and R. Quinn, "Fatigue life and frequency response of braided pneumatic actuators," in *Proc. IEEE Int. Conf. Robot. Autom.*, vol. 3, pp. 2830–2835 vol.3, 2002.

[39] S. Li, D. M. Vogt, D. Rus, and R. J. Wood, "Fluid-driven origami-inspired artificial muscles," *Proc. Natl. Acad. Sci. USA*, vol. 114, no. 50, pp. 13132–13137, 2017.

[40] D. Yang, M. S. Verma, J.-H. So, B. Mosadegh, C. Keplinger, B. Lee, F. Khashai, E. Lossner, Z. Suo, and G. M. Whitesides, "Buckling pneumatic linear actuators inspired by muscle," *Adv. Mater. Technol.*, vol. 1, no. 3, p. 1600055, 2016.